



OPEN

Electrostatic doping as a source for robust ferromagnetism at the interface between antiferromagnetic cobalt oxides

Zi-An Li¹, N. Fontañá-Troitiño², A. Kovács³, S. Liébana-Viñas^{1,2}, M. Spasova¹, R. E. Dunin-Borkowski³, M. Müller⁴, D. Doennig⁴, R. Pentcheva^{1,4}, M. Farle¹ & V. Salgueiriño²

SUBJECT AREAS:

DENSITY FUNCTIONAL
THEORYMAGNETIC PROPERTIES AND
MATERIALS

NANOSCALE MATERIALS

Received
1 October 2014Accepted
31 December 2014Published
23 January 2015Correspondence and
requests for materials
should be addressed to
M.F. (michael.farle@
uni-due.de)

¹Faculty of Physics and Center for Nanointegration (CENIDE), University of Duisburg-Essen 48047, Duisburg (Germany), ²Departamento de Física Aplicada, Universidade de Vigo 36310, Vigo (Spain), ³Ernst Ruska-Centre and Peter Grünberg Institute, Research Centre Jülich, 52425 Jülich, (Germany), ⁴Department of Earth and Environmental Sciences, Section Crystallography, LMU Munich, Theresienstr. 41, 80333 Munich (Germany).

Polar oxide interfaces are an important focus of research due to their novel functionality which is not available in the bulk constituents. So far, research has focused mainly on heterointerfaces derived from the perovskite structure. It is important to extend our understanding of electronic reconstruction phenomena to a broader class of materials and structure types. Here we report from high-resolution transmission electron microscopy and quantitative magnetometry a robust – above room temperature (Curie temperature $T_C \gg 300$ K) – environmentally stable-ferromagnetically coupled interface layer between the antiferromagnetic rocksalt CoO core and a 2–4 nm thick antiferromagnetic spinel Co_3O_4 surface layer in octahedron-shaped nanocrystals. Density functional theory calculations with an on-site Coulomb repulsion parameter identify the origin of the experimentally observed ferromagnetic phase as a charge transfer process (partial reduction) of Co^{3+} to Co^{2+} at the CoO/ Co_3O_4 interface, with Co^{2+} being in the *low spin* state, unlike the high spin state of its counterpart in CoO. This finding may serve as a guideline for designing new functional nanomagnets based on oxidation resistant antiferromagnetic transition metal oxides.

Functional oxide interfaces based on transition metal oxides¹ have been recognized for their new and exciting fundamental physics^{2,3} as well as for their potential as next-generation nanoelectronic materials. They are associated with a wide variety of interesting physical phenomena, such as superconductivity, ferroelectricity, ionic conduction and magnetism. Given the success that has been achieved in finding novel properties for technological applications in systems such as perovskite-type $\text{LaAlO}_3/\text{SrTiO}_3$ oxide interfaces⁴, it becomes important to also find further promising material combinations and structure types that may exhibit exotic properties. For example, a surprising lamellar ferromagnetic order at intergrowths of antiferromagnetic (AFM) haematite (Fe_2O_3) and para/antiferromagnetic (PM/AFM) ilmenite (FeTiO_3) has been reported^{5,6}. The charge imbalance at the interface has been identified as a source of this phenomenon, very often accompanied by local distortions. This can induce charge transfer processes and change the bond-angles between ions. These effects modify the competing ferromagnetic (FM) and AFM interactions (super-exchange, and double exchange) in antiferromagnets as described by the so called Goodenough-Kanamori-Anderson (GKA) rules⁷. For instance a distortion (bond-angle change) and charge transfer can turn the AFM 180° magnetic ion-oxygen-magnetic ion superexchange of partially filled 3d e_g (d_z^2 , $d_{x^2-y^2}$) or t_{2g} (d_{xy} , d_{yz} , d_{zx}) orbitals into ferromagnetic (double) exchange. Consequently, tuning the relative magnitudes of competing magnetic interactions via strain control at interfaces opens a promising route to create new types of magnets.

The interesting question arises if ferromagnetic order can be stabilized between two simple antiferromagnets like CoO and Co_3O_4 , both of which are antiferromagnets with ordering temperatures $T_N = 291$ K and 40 K, respectively^{8,9}. In nanostructured AFM materials¹⁰ pairing of the two mutually compensating ferromagnetic sublattices is broken due to surface rearrangement, which leads to the presence of “uncompensated” and often “frustrated” surface moments and the consequent magnetic reconstruction¹¹. Several examples of weak ferromagnetism in nanoparticulate CoO^{12–14} and Co_3O_4 ^{15–17} materials have been reported in the literature based on these explanations, though the irregular shapes and the relatively wide size distributions of nanoparticles have made a detailed analysis of the origin of the observed ferromagnetic response very difficult. In contrast, nearly perfect antiferromagnetic CoO nanocrystals with octahedron shapes and different average sizes, as reported in



Ref. 18, should allow the origin of the room temperature ferromagnetism to be identified. These crystalline CoO octahedra have eight (111) crystal facets stabilized by a thin Co₃O₄ shell, which forms naturally by surface oxidation in air^{19–21}, and is thermodynamically more stable than CoO. The uncompensated magnetic moments in the ~3 nm thick AFM Co₃O₄ surface layer have been assumed as a likely source of the observed ferromagnetism. However, the origin of a quasi two-dimensional long-range ferromagnetic order persisting in a temperature range where the AFM CoO and Co₃O₄ bulk phases are paramagnetic is not understood.

Here, we demonstrate that the atomically sharp interface between the crystalline ~3 nm thick spinel-type Co₃O₄ surface layer and the crystalline CoO (rocksalt structure) is the source of the ferromagnetism observed up to 400 K. The octahedron-shaped nanocrystals with edge lengths between 40 and 150 nm, have a heavily strained epitaxial CoO/Co₃O₄ interface that forms at the eight (111) facets, offering quasi-2D ferromagnetic interfaces stable even in the paramagnetic regime of the antiferromagnetic CoO ($T > 291$ K). Using a combination of magnetometry, transmission electron microscopy and density functional theory (DFT) we obtain quantitative results confirming that an electronic reconstruction accompanied by a considerable interlayer compression of the CoO oxide (111) layer spacing at the interface to the Co₃O₄ surface coating explains the ferromagnetic order and its stability. One may note that such an enhanced T_C in a quasi 2D interface is remarkable, since lower dimensionality in general expected to lead to enhanced thermal fluctuations and a reduced ordering temperature²². Consequently, our results show that the occurrence of magnetic order in these octahedron-shaped nanocrystals can be attributed to the changes of bond-angles and valence states at the (111) CoO/Co₃O₄ interface, which modify the relative strengths of the inherent *ferromagnetic* double exchange and *antiferromagnetic* superexchange.

CoO crystallizes in the cubic rocksalt-structure, $Fm\bar{3}m$ (O_h^5), above the Néel temperature $T_N = 291$ K, in which alternating layers of (111) Co planes with opposite magnetization directions are separated by oxygen planes. The Co²⁺ ions occupy the octahedral sites formed by the faced-centered-cubic (FCC) arranged O²⁻ ions. Below T_N the magnetic order induces a transition to a monoclinic phase ($C2/m$ (C_{2h}^3))²³. This results in a distorted octahedral crystal field with a spin $S = 3/2$ and an unquenched orbital momentum of approximately $L = 1$ ($L/S = 0.7$)²⁴ in the antiferromagnetically ordered state. AFM CoO has a very high magnetocrystalline anisotropy constant of $\sim 2.7 \times 10^7$ J cm⁻³²⁵, which is comparable to that of the hard magnet samarium-cobalt²⁶. In thin CoO layers the single ion magnetic anisotropy energy (MAE) density was found to change from 4.8 meV/atom to -1.6 meV/atom upon dilating or compressing along the CoO(100) plane and has been related to a large change of electronic occupation of the e_g and t_{2g} orbital states²⁷. In principle, an ideal CoO crystal slab in a (111) orientation could show two contributions: a vanishing total magnetization for an even number of Co layers and the magnetization of a single Co²⁺ monolayer for an odd number of Co layers. On the other hand, the modified crystal field symmetry at the surface due to a missing or relaxed O²⁻ surface layer changes the octahedral (O_h) symmetry dramatically, can unquench the orbital momentum and can consequently modify the spin only magnetic moment $S = 3/2$ with $\mu_S = g\sqrt{S(S+1)}\mu_B = 3.9\mu_B$. Unfortunately, such ideal surface layers cannot be stabilized due to their high polarity. As shown for Co (111) films grown on Ir(100), nature circumvents the polarity problem by an appropriate surface reconstruction, that is, by switching from the rocksalt type to wurtzite-type stacking near the surface, which turns out to become metallic at the interface in ultra-high vacuum²⁸.

Co₃O₄ crystallizes in the normal spinel structure with the general formula $[A]^{tet}[B_2]^{oct}O_4$, that is, $[Co^{2+}]^{tet}[Co_2^{3+}]^{oct}O_4$. Co³⁺ ions (“B” sites, 3d⁶, spin $S = 0$) occupy octahedral sites and Co²⁺ ions occupy the tetrahedral (“A”) sites formed by O²⁻ species yielding an

$S = 3/2$ state. The Co²⁺ ions on the A site are antiferromagnetically ordered below 40 K, namely, each ion at a tetrahedral site “A” is surrounded by four nearest neighbor A sites with an antiparallel magnetic moment. The $[Co^{3+}]^{oct}$ ions on the B site are in the low spin (LS) $S = 0$ state, i.e., diamagnetic.

Cobalt oxide octahedron-shaped nanocrystals (Fig. 1a) prepared by colloidal chemistry (described in the Methods section) offer the possibility to study changes in interface structure, electronic properties and competing magnetic interactions. X-ray powder diffraction, neutron diffraction and X-ray photoemission spectroscopy measurements revealed that the major constituent of these nanocrystals was CoO with a rocksalt structure at room temperature and confirmed the absence of metallic (Co⁰) cobalt. High-resolution TEM measurements revealed the CoO-Co₃O₄ core-shell structure of the nanoparticles. Figure 1a shows a bright-field TEM image of the as-synthesized CoO nanocrystals deposited on an amorphous carbon support film. The observed morphologies of the nanocrystals, which take the form of hexagons, rectangles and rhombi in 2D projection, originate from 3D octahedral particle shapes (confirmed using electron tomography) whose crystal facets are determined by the underlying cubic crystallographic structure (see the scheme in Fig. 1b). The average edge lengths of the octahedron-shaped nanocrystals were determined to be 40 ± 8 nm and 75 ± 10 nm from bright-field TEM images. In the following, these samples are referred to as S-40 nm and S-75 nm, respectively.

Magnetic characterization of the CoO nanostructures was performed using a SQUID magnetometer under zero-field cooling (ZFC) and field cooling (FC) conditions. The measured field-dependent magnetization $M(H)$ showed clear hysteresis loops (Fig. 1c,d) at $T = 300$ K and 5 K, with characteristics of ferromagnetic behavior, superimposed on the expected paramagnetic ($T = 300$ K) and antiferromagnetic ($T = 5$ K) linear field-dependent response of CoO and Co₃O₄. The saturation magnetization $M_S = 1.58$ Am²/kg (Co metal: 163.6 Am²/kg), the remanent magnetization $M_R = 0.261$ Am²/kg, and the coercivity $H_C = 35.7$ mT measured at 300 K for the S-75 nm sample (Fig. 1c) unambiguously indicate a ferromagnetically ordered component in the nominally purely paramagnetic state above the Néel temperature $T_N = 291$ K of CoO, which forms the core of every octahedron. Another unambiguous proof for the interfacial coexistence of FM and AFM components is the observation of an exchange bias field H_{EB} at lower temperatures, seen as the horizontal and vertical shift of the hysteresis after field cooling (FC) relative to the ZFC $M(H)$ loop (Fig. 1d). The temperature-dependence of the exchange bias field H_{EB} and of the coercive field H_C for samples S-40 nm and S-75 nm (Fig. S1) shows that H_{EB} vanishes above $T_N^{CoO} = 291$ K as expected, while the coercive field $\mu_0 H_C$ is still larger than about 30 mT. A detailed summary of the variation in M_S , M_R and H_C with temperature for the ZFC and FC $M(H)$ experiments is given in Supplementary Tables T1 and T2. In addition, K-edge X-ray absorption spectra, neutron diffraction studies, and temperature dependent susceptibility measurements confirmed the absence of metallic cobalt and the existence of crystalline antiferromagnetic CoO with $T_N^{CoO} = 291$ K and a thin shell of Co₃O₄ with a finite-size-effect reduced $T_N = 20$ K¹⁸.

The reduced - mass normalized - saturation magnetization M_S measured for the smaller octahedra S-40 nm (2.81 Am²/kg at 5 K and 2.60 Am²/kg at 300 K) in comparison to the S-75 nm octahedra (1.72 Am²/kg at 5 K and 1.55 Am²/kg at 300 K) suggests that a surface or interface contribution is the origin of the ferromagnetic response. To support this analysis, we have calculated the expected magnetization of ferromagnetic single and double surface or interface layers of Co²⁺ ions. The number of these Co²⁺ cations at the apexes, edges, surfaces, and interfaces was estimated for a given size and shell thickness of a CoO-Co₃O₄ core-shell octahedron, by making use of the geometrical relationship between the rocksalt-spinel crystal structures and the octahedral morphology. For an octahedral

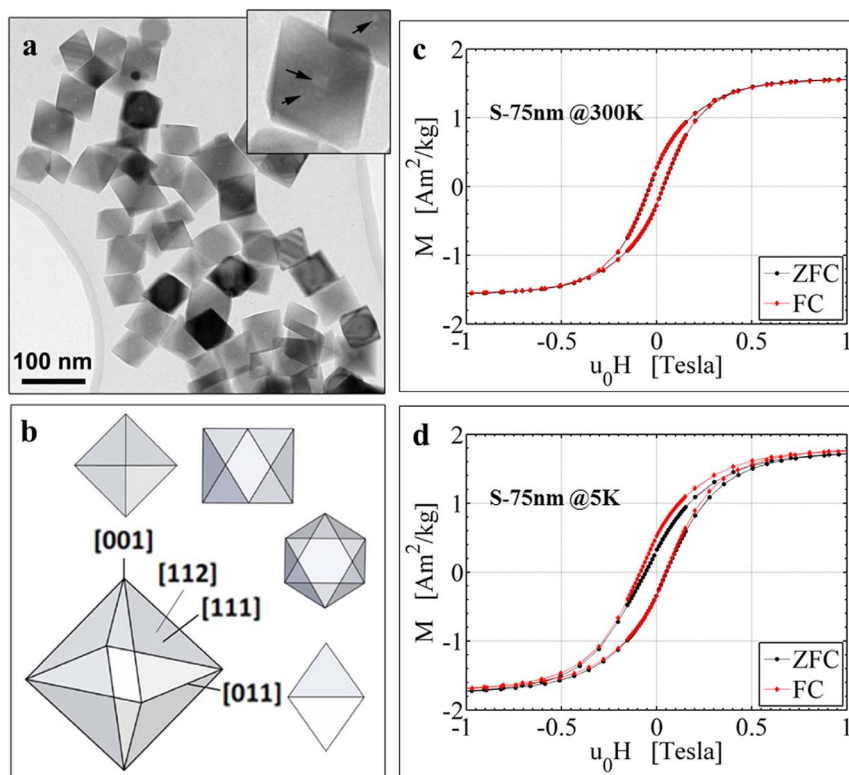


Figure 1 | TEM and magnetic characterization of octahedral cobalt oxide nanocrystals. (a), TEM bright-field image of octahedral cobalt oxide nanocrystals on an amorphous C support film. The particles exhibit patches of brighter contrast, which are likely to be related to the presence of voids inside the particles, as indicated by arrows in the inset. (b), Schematic representation of the octahedral particle shape, its projections and the corresponding crystallographic orientations for a cubic crystal structure. (c), ZFC and FC hysteresis loops, recorded at 300 K from samples S-75 nm and shown after subtraction of the linear paramagnetic (300 K) component. (d), As for c but at $T = 5$ K, the FC magnetization curve is shifted horizontally to the left relative to the ZFC curve. Values of H_C , M_R and M_S (see text) are given in Tables T1 and T2.

particle with eight 111 facets (Fig. 2b), where the number of atoms along the 111 facet is n , the number of Co^{2+} cations at the apexes is 6, at the edge is $12(n - 1)$, at the surfaces is $8[(n - 1)(n - 4)/2 + 1]$, and in the inside volume is $(2n^2 + 1)/3$. Taking the typical magnetic moment $\mu = (4.8 \pm 0.4)\mu_B$ for Co^{2+29} , we calculate the saturation magnetization M_S for one layer (blue curves) of surface Co^{2+} cations (see Fig. 2a), while the red curves show the calculated values of M_S for a double-layered interface of Co^{2+} . The red curves intersect the measured M_S (black solid and dashed lines for 300 K and 5 K) for the S-40 nm sample at a size range of 38–45 nm, while for S-75 nm the intersection occurs at a size range of 60–80 nm. The striking match between the measured and calculated saturation magnetization must therefore be associated with interfacial ferromagnetic long-range order, and not surface-derived ferromagnetism.

In order to understand the reason for the appearance of this interfacial long-range ferromagnetic order, we have also performed high-angle annular dark field (HAADF) imaging. Figure 3a shows an atomically resolved HAADF image of the edge of a typical cobalt oxide octahedron, oriented along the [110] direction. In HAADF imaging, the recorded contrast arises primarily from Rutherford and thermal diffuse scattering³⁰. Under our experimental conditions, the HAADF intensity scales to a good approximation with the atomic number $Z^{1.7}$ and the specimen thickness, since the area of interest is sufficiently thin. A distinct core-shell contrast variation with different atom-column configurations is appreciated. Figure 3b shows an enlargement of the interface area outlined by a dashed-square in Fig. 3a, in which a (111)-type interface and (002)-type interfaces between CoO and Co_3O_4 (delineated by dashed lines) can be identified. The core region (A) corresponds to a [110] atomic column projection of the rocksalt CoO structure, while the shell region (B)

corresponds to a [110] atomic column projection of the normal spinel Co_3O_4 structure. The bright contrast corresponds to cobalt cation columns, whose scattering strength is greater than that of oxygen anions. For more precise atomic lattice information, we have analyzed the intensity variation and lattice spacing in different HAADF images. The rectangular a–b area shown in Fig. 3b was selected for intensity profile analysis (not shown) and indicates a clear intensity variation that reflects structure and chemistry differences across the interface boundaries. By using the CoO core as a reference, we measured variations of the (111)-plane lattice spacing in the CoO/ Co_3O_4 interface region. The measurements (red data points in Fig. 3c) revealed a progressive decrease in lattice spacing from the core to the surface by as much as 8%, suggesting the presence of large strain in the interface region. Within experimental accuracy, we find that the Co_3O_4 plane spacing (235 pm) is bulk-like and stays unchanged. Only the CoO (111) spacing is strongly compressed at the interface and relaxes towards the core within three to four layers to its respective bulk value.

To shed more light on the underlying mechanisms DFT+\$\text{US}\\$ calculations were performed considering two different terminations of Co_3O_4 at the interface: one with exclusively octahedral Co (named B-layer) and one with a mixed octahedral, tetrahedral layer. The calculated lattice spacings (blue data points in Fig. 3c) match very well the experimentally measured ones confirming that the interlayer distances on the CoO side of the interface are strongly reduced, while on the Co_3O_4 side it is close to the bulk-value. The very good agreement between the theoretical and experimental interlayer distances shown in Fig. 3d for the B-layer model unambiguously identifies that the latter is realized at the interface.

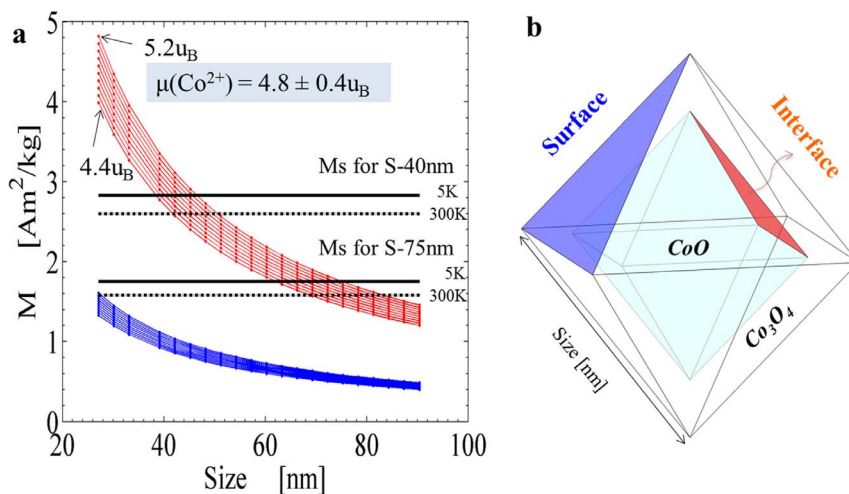


Figure 2 | (a) Size dependence of experimentally measured (black solid ($T = 5$ K) and dashed (300 K) lines) and calculated saturation magnetization M_S of CoO octahedra. A magnetic moment μ of $(4.8 \pm 0.4)\mu_B$ per Co^{2+} ion and a shell thickness of 3 nm Co_3O_4 is assumed. M_S arises only from the Co cations at the surfaces or interfaces of the octahedral nanocrystals, as indicated in the schematic in (b). The blue lines are calculated values assuming only effectively one layer of Co^{2+} cations at the Co_3O_4 surface, while the red lines correspond to a double layer of Co cations at the interface, as discussed in the text.

Below the side view of the relaxed structure from DFT+ U calculations in Fig. 3d), Fig. 3e) shows the spin density and orbital polarization of the heterostructure. Red and blue contours denote antiparallel orientations of magnetic moments. Besides the antiferromagnetically ordered octahedral Co^{2+} in CoO and tetrahedral Co^{2+} in Co_3O_4 , a striking feature is the noticeable spin density at the Co^{3+} sites (we note that no spin density is observed in bulk Co_3O_4 – not shown here). While the total contribution of the red and blue lobes at Co^{3+} in the inner layers sums up to a relatively small spin magnetic moment of $0.05 \mu_B$, individual octahedral Co-sites at the interface adopt a considerable magnetization of $0.4\text{--}0.8 \mu_B$ (for details see Methods). This high magnetic moment signals a valence change from Co^{3+} towards Co^{2+} at the interface. Most importantly, these sites are in a low spin (LS) state, unlike Co^{2+} in the CoO part of the superlattice. The latter are in a high spin (HS) state with magnetic moments of $2.58 \mu_B$ (close to the value of $2.64 \mu_B$ in bulk CoO). Thus, the interface magnetism originates from a change in oxidation state at the octahedral sites with a LS state, which is clearly distinct from the HS state in bulk CoO.

By making use of the interfacial atomistic information obtained from the HAADF image analysis and the DFT + U calculations, it is possible to draw conclusion about the atomic interface structure of the two cobalt oxides. As mentioned above in bulk rocksalt CoO, Co^{2+} cations occupy octahedral sites in a lattice of FCC O^{2-} ions. In contrast, in bulk normal spinel Co_3O_4 , Co^{3+} cations populate half of the octahedral sites, while Co^{2+} cations populate one-eighth of the tetrahedral sites in an FCC lattice of O^{2-} ions. The two structures can be epitaxially matched at the (111) facets of the FCC sublattice of host O^{2-} ions, when the bulk lattice mismatch of about 5% (4.261 \AA for CoO: JCPDS card no. 48-1719 and 8.084 \AA for Co_3O_4 : JCPDF card no. 42-1467) can be accommodated by strain. Such “flexible” accommodation of cobalt cations to form different oxides has also been observed in other transition metal oxide systems. Consequently, one can construct rocksalt/spinel (111)-type interfaces. In this model, the interfacial oxygen plane is adjacent to octahedral $\text{Co}^{2+}_{\text{oct}}$ ($S = 3/2$) in CoO and octahedral $\text{Co}^{3+}_{\text{oct}}$ ($S = 0$) in Co_3O_4 . To understand the appearance of ferromagnetism we can compare the interface structure to an inverse spinel structure, which is typical for example for ferrimagnetic Fe_3O_4 . The difference between $([\text{Co}^{2+}]_{\text{tet}}[\text{Co}^{3+}]_{\text{oct}})_4\text{O}_4^{2-}$ and $([\text{Fe}^{3+}]_{\text{tet}}[\text{Fe}^{2+}]_{\text{oct}})_4\text{O}_4^{2-}$ is the valence of the cobalt and iron cations in their respective tetrahedral and octahedral environments. In Fe_3O_4 , magnetic super

exchange (SE) and double exchange (DE) interactions between iron cations and their inequivalent neighbors proceed via the same oxygen anion. The $\text{Fe}^{2+}_{\text{oct}}$ and $\text{Fe}^{3+}_{\text{oct}}$ cations are coupled ferromagnetically through double exchange (DE). However, the two $\text{Fe}^{3+}_{\text{tet}}$ and $\text{Fe}^{3+}_{\text{oct}}$ cations are coupled antiferromagnetically through super exchange (SE), such that their moments of $\pm 5 \mu_B$ cancel. An unpaired moment of $4 \mu_B$ on the $\text{Fe}^{2+}_{\text{oct}}$ cation site remains. Consequently, Fe_3O_4 exhibits ferrimagnetic behavior with a high Curie temperature $T_C = 858 \text{ K}$ ³¹. In Co_3O_4 , on the other hand, the weak tetrahedral-tetrahedral (T-T) AFM interactions between the $\text{Co}^{2+}_{\text{tet}}$ cations lead to antiferromagnetism⁹ with a low ordering temperature T_N of $\sim 20\text{--}40 \text{ K}$. Consequently, a ferromagnetic order with a high Curie temperature can be stabilized at the interface if magnetic moments are present at both the octahedral and the tetrahedral sites. Such a scenario was previously explained by a transition from a normal to inverse spinel in Co_3O_4 nanoparticles by Chen *et al.*³² and by Serrano *et al.*¹⁶ at the surfaces of nanoparticles on TiO_2 . On the other hand, our results demonstrate a rather different mechanism of formation of $\text{Co}^{2+}_{\text{oct}}$ at the interface with an unanticipated low spin state of $S = 1/2$. In the study of Serrano *et al.*¹⁶, a weak FM signal was attributed to surface reduction of $\text{Co}^{3+}_{\text{oct}}$ to $\text{Co}^{2+}_{\text{oct}}$, whereby complex magnetic interactions involving T-T ($\text{Co}^{2+}_{\text{tet}} - \text{Co}^{2+}_{\text{tet}}$), O-O ($\text{Co}^{3+}_{\text{oct}} - \text{Co}^{2+}_{\text{oct}}$) and T-O could occur, in analogy to that in Fe_3O_4 . Here, we suggest that it is possible to achieve long-range ferromagnetic order with a high Curie temperature due to the coupling of $\text{Co}^{2+}_{\text{oct}}$ ($S = 3/2$ and $1/2$) and $\text{Co}^{2+}_{\text{tet}}$ cations on both sides of the epitaxial interface, as shown in Fig. 3d) and e). Our experimental and computational results indicate that robust ferromagnetic order can occur at (111) interfaces between CoO and Co_3O_4 above the highest Neel temperature of the antiferromagnets. To understand that such a behavior was not observed in previous Co oxide thin film studies, one may consider lateral size effects in the nanocrystals. These may be important to prevent the formation of strain-releasing misfit dislocations at the interface – as has also been found in the growth of nanowires with heavily strained semiconductor heterostructures³³. It will be interesting to investigate in the future, if defect-free CoO/ Co_3O_4 interfaces could be stabilized in laterally extended epitaxial thin films despite the large strain observed in the CoO interface layers.

In summary, the present rocksalt/spinel-type system provides a fascinating oxide interface, in which electrostatic doping can induce changes of competing magnetic interactions (SE and DE) at the

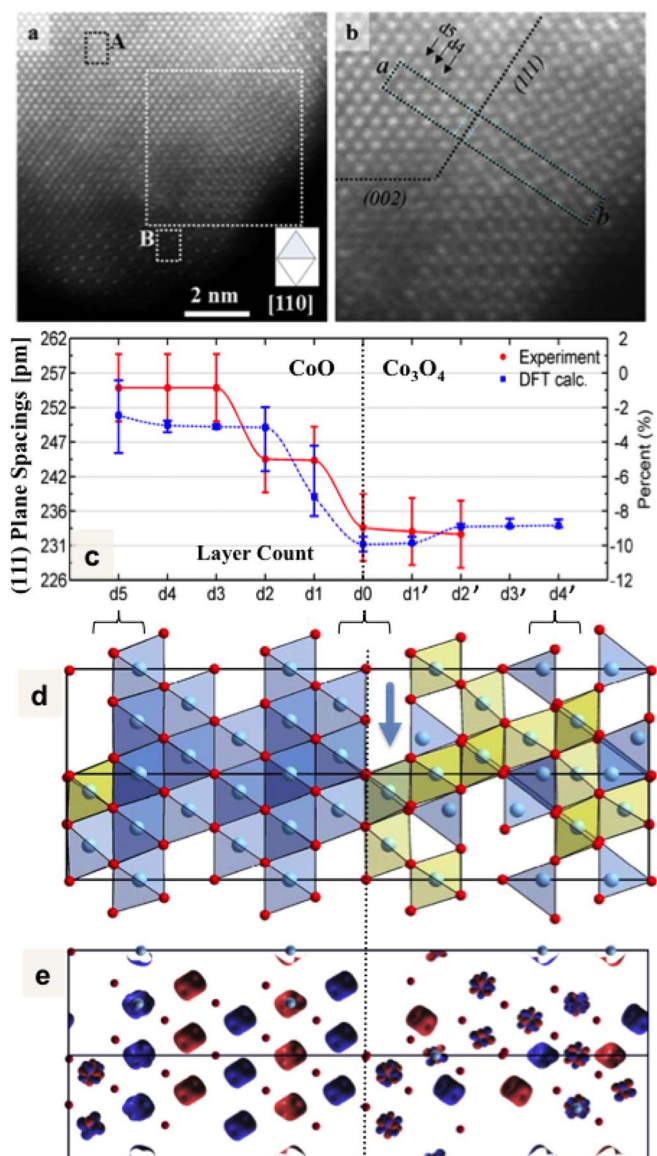


Figure 3 | STEM-HAADF image of a single octahedral cobalt oxide nanocrystal. (a), Atom-column-resolved STEM-HAADF image of the edge of a [1–10]-oriented cobalt oxide nanocrystal acquired in STEM mode at 80 kV using a probe size of ~ 0.1 nm. The core region A and the shell region B exhibit contrast characteristic of [1–10]-oriented CoO and Co_3O_4 respectively. (b), Enlargement of the interface area: (111)-type interface between a CoO core and the Co_3O_4 shell. (c), Measured (red dots) and calculated (blue dots) lattice plane spacings as a function of spacing number near the interface. “d0” denotes the spacing indicated by the dashed line in b. (d), Side view of the relaxed geometry of the CoO/ Co_3O_4 (111) heterostructure obtained from the DFT + U calculations. The interface plane (dashed line) of O^{2-} (red dots) connects octahedral Co ions (blue dots) in Co_3O_4 on the right to octahedral Co^{2+} ions in CoO on the left. Co^{2+} and Co^{3+} are denoted by blue/yellow polyhedra. As discussed in the text, electronic reconstruction in the interface Co_3O_4 layer reduces the $S = 0$ [Co^{3+}] $_{\text{oct}}$ to low spin [Co^{2+}] $_{\text{oct}}$. (e), Spin density of the CoO/ Co_3O_4 (111) heterostructure obtained from the DFT + U calculations. Red and blue contours denote antiparallel orientations of magnetic moments. Besides the antiferromagnetic alignment of octahedral Co^{2+} in CoO and tetrahedral Co^{2+} in Co_3O_4 , note a considerable spin density at the Co^{3+} sites in the inner Co_3O_4 layers (not present in bulk Co_3O_4). A key feature is the significant spin polarization in the interface Co_3O_4 signaling the reduction of octahedral Co^{3+} to Co^{2+} sites in an unanticipated low spin state ($S = 1/2$) – the corresponding sites are emphasized by the arrow.

nanoscale level. We provide experimental and theoretical results to explain the appearance of a robust ferromagnetic order with a Curie temperature above 400 K at the epitaxial (111) interface of the two antiferromagnets CoO and Co_3O_4 . We suggest that the electrostatic doping at the polar interface leading to an electronic reconstruction³⁴ with a valence change, accompanied by an unanticipated spin state, is the origin of the effective long-range ferromagnetic order. As Co_3O_4 exhibits extraordinary catalytic activity for the oxidation of carbon monoxide and hydrocarbons and thus has the potential to at least partly replace noble metals or rare earth materials in technologically relevant processes, such ferromagnetic nano-octahedra with catalytic shell may become useful in technologies in which the particles can be recollected by magnetic gradient fields for reactivation.

Methods

CoO nanooctahedra were obtained using the hot-injection thermodecomposition of cobalt acetate (Sigma-Aldrich, 98%), (2.66 and 4 mmol) (dissolved in 5 mL of ethanol) in trioctylamine (Aldrich, 90%) (25 mL, 57.18 mmol) and oleic acid (Aldrich, 90%) (5.12 and 8 mmol) at 170°C and then left to reflux (at $T = 300^\circ\text{C}$) for two hours. Once cooled to room temperature, the nanocrystals were obtained by centrifugation, washed several times and stored in ethanol. Repeated syntheses confirm the reproducibility of the final products.

Specimens for TEM analysis were prepared by dropping the diluted colloidal solution onto copper grids covered with a thin (~ 10 nm) amorphous carbon film and by allowing the solvent to evaporate. Structural and chemical characterization of the cobalt oxide nanocrystals was performed using several transmission electron microscopes. An FEI Titan 80–300 TEM operated at 200 kV was used for high-resolution TEM analysis (not shown here). An FEI Titan Ultimate 60–300 TEM operated at 80 kV was used for STEM EEL spectroscopy and atom-column-resolved STEM HAADF imaging. EEL spectra were acquired in STEM mode using a ~ 1 nm electron probe with an energy resolution of ~ 0.8 eV or better, as evaluated from the full-width at half-maximum of the zero-loss peak. Spectra were recorded using a dispersion of 0.3 eV/channel and acquisition time of 0.5 s for each spectrum image to minimize electron irradiation damage. The convergence and collection semi-angles were estimated to be 20 and 26.5 mrad, respectively. Magnetic characterization was performed using a SQUID magnetometer. Possible sources of error include sample preparation, post-treatment processing, and sample storage. We also checked the possible ageing effect on magnetic properties of the samples and found negligible change in $M(H)$ and $M(T)$ for both samples kept under ambient conditions for a duration of six months.

First principles calculation. DFT calculations were performed using the all-electron full-potential linearized augmented plane wave (FP-LAPW) method, as implemented in the WIEN2k code^{35,36}. For the exchange-correlation potential we used the generalized gradient approximation GGA³⁷ with an on-site Coulomb repulsion term $U_{\text{Co}} = 5$ eV (LDA/GGA + U method³⁸). The muffin-tin spheres of the atoms were chosen as: 1.8 (Co) and 1.6 a.u. (O), respectively. The following cutoffs were used: $E_{\text{max}}^{\text{wf}} = 19$ Ry for the plane wave representation in the interstitial region; $G_{\text{max}} = 12$ (a.u.) $^{-1}$ for the plane wave expansion of the charge density and $l_{\text{max}} = 10$ for spherical harmonics inside the muffin-tin spheres. The integrals in reciprocal space were performed with 52 k -points in the irreducible part of the Brillouin zone (IBZ). The CoO/ Co_3O_4 (111) heterostructure is modeled using six layers (and 2×2 lateral units) of CoO and one unit cell of Co_3O_4 , using the lateral lattice parameter CoO ($a_{\text{CoO}} = 6.02$ Å). The atomic positions are fully relaxed within hexagonal symmetry. Three different systems were considered, depending on the interface termination of Co_3O_4 with either an octahedral layer or a mixed octahedral/tetrahedral termination. The very good agreement in interlayer spacing between experiment and the B-layer model, identifies the latter as the preferred termination. The results for this interface are presented in Fig. 3d–e. Note that the heterostructure contains two B-layer interfaces on both sides of Co_3O_4 . Because no symmetry constraints are imposed in the calculation and the stacking of layers is not identical at both sides we obtain a slight asymmetry of the interfaces, expressed in a difference of magnetic moments (0.4 and 0.8 μ_B) at the interfacial Co^{2+} oct sites, however the general mechanism of reduction of octahedral Co and a low spin state is present at both interfaces.

- Miletto Granozio, F., Koster, G. & Rijnders, G. Functional oxide interfaces. *MRS Bull.* **38**, 1017–1023 (2013).
- Imada, M., Fujimori, A. & Tokura, Y. Metal-insulator transitions. *Rev. Mod. Phys.* **70**, 1039–1263 (1998).
- Tokura, Y. & Nagaosa, N. Orbital Physics in Transition-Metal Oxides. *Science* **288**, 462–468 (2000).
- Hwang, H. Y. *et al.* Emergent phenomena at oxide interfaces. *Nat. Mater.* **11**, 103–113 (2012).
- Robinson, P., Harrison, R. J., McEnroe, S. A. & Hargreaves, R. B. Lamellar magnetism in the haematite – ilmenite series as an explanation for strong remanent magnetization. *Nature* **418**, 517–520 (2002).



6. Nabi, H. S., Harrison, R. J. & Pentcheva, R. Magnetic coupling parameters at an oxide-oxide interface from first principles: Fe₂O₃-FeTiO₃. *Phys. Rev. B* **81**, 214432 (2010).
7. Geertsma, W. & Khomskii, D. Influence of side groups on 90 degrees superexchange: A modification of the Goodenough-Kanamori-Anderson rules. *Phys. Rev. B. Condens. Matter* **54**, 3011–3014 (1996).
8. Roth, W. L. Magnetic structures of MnO, FeO, CoO and NiO. *Phys. Rev.* **110**, 1333–1341 (1958).
9. Roth, W. L. The magnetic structure of Co₃O₄. *J. Phys. Chem. Solids* **25**, 1–10 (1964).
10. Néel, L. Superparamagnetism of very small antiferromagnetic particles. *Comptes Rendus* **252**, 4075 (1961).
11. Benitez, M. *et al.* Evidence for Core-Shell Magnetic Behavior in Antiferromagnetic Co₃O₄ Nanowires. *Phys. Rev. Lett.* **101**, 097206 (2008).
12. Zhang, L., Xue, D. & Gao, C. Anomalous magnetic properties of antiferromagnetic CoO nanoparticles. *J. Magn. Magn. Mater.* **267**, 111–114 (2003).
13. Dutta, D. P., Sharma, G., Manna, P. K., Tyagi, A. K. & Yusuf, S. M. Room temperature ferromagnetism in CoO nanoparticles obtained from sonochemically synthesized precursors. *Nanotechnology* **19**, 245609 (2008).
14. Yang, G. *et al.* Room Temperature Ferromagnetism in Vacuum-Annealed CoO Nanospheres. *J. Phys. Chem. C* **114**, 21989–21993 (2010).
15. Nethravathi, C. *et al.* Ferrimagnetic Nanogranular Co₃O₄ through Solvothermal Decomposition of Colloidally Dispersed Monolayers of α -Cobalt Hydroxide. *J. Phys. Chem. B* **109**, 11468–11472 (2005).
16. Serrano, A. *et al.* Room-temperature ferromagnetism in the mixtures of the TiO₂ and Co₃O₄ powders. *Phys. Rev. B* **79**, 144405 (2009).
17. Lv, P., Zhang, Y., Xu, R., Nie, J.-C. & He, L. Anomalous magnetic properties of 7 nm single-crystal Co₃O₄ nanowires. *J. Appl. Phys.* **111**, 013910 (2012).
18. Fontañá-Troitiño, N. *et al.* Room-temperature ferromagnetism in antiferromagnetic cobalt oxide nanooctahedra. *Nano Lett.* **14**, 640–7 (2014).
19. Langell, M., Anderson, M., Carson, G., Peng, L. & Smith, S. Valence-band electronic structure of Co₃O₄ epitaxy on CoO(100). *Phys. Rev. B* **59**, 4791–4798 (1999).
20. Kant, C. *et al.* Optical spectroscopy in CoO: Phononic, electric, and magnetic excitation spectrum within the charge-transfer gap. *Phys. Rev. B* **78**, 245103 (2008).
21. Wang, H.-Q., Altman, E. & Henrich, V. Interfacial properties between CoO (100) and Fe₃O₄ (100). *Phys. Rev. B* **77**, 085313 (2008).
22. Li, Y., Farle, M. & Baberschke, K. Critical spin fluctuations and Curie temperature of ultrathin Ni(111) W(110): A magnetic-resonance study in ultrahigh vacuum. *Phys. Rev. B* **41**, 9596–9599 (1990).
23. Schrön, A., Rödl, C. & Bechstedt, F. Crystalline and magnetic anisotropy of the 3d-transition metal monoxides MnO, FeO, CoO, and NiO. *Phys. Rev. B* **86**, 115134 (2012).
24. Ney, A. *et al.* Absence of Intrinsic Ferromagnetic Interactions of Isolated and Paired Co Dopant Atoms in Zn_{1-x}CoxO with High Structural Perfection. *Phys. Rev. Lett.* **100**, 157201 (2008).
25. Kanamori, J. Theory of the magnetic properties of ferrous and cobaltous oxides. *Prog. Theor. Phys.* **17**, 177–196 (1957).
26. Becker, J. J. Rare earth compound permanent magnets. *J. Appl. Phys.* **41**, 1055–1064 (1970).
27. Csiszar, S. I. *et al.* Controlling Orbital Moment and Spin Orientation in CoO Layers by Strain. *Phys. Rev. Lett.* **95**, 187205 (2005).
28. Heinz, K. & Hammer, L. Epitaxial cobalt oxide films on Ir(100)-the importance of crystallographic analyses. *J. Phys. Condens. Matter* **25**, 173001 (2013).
29. Kittel, C. *Introduction to Solid State Physics*. (John Wiley & Sons, Inc., 2005).
30. Batson, P. E., Dellby, N. & Krivanek, O. L. Sub-ångstrom resolution using aberration corrected electron optics. *Nature* **418**, 617–620 (2002).
31. Stöhr, J. & Siegmann, H. C. *Magnetism From Fundamentals to Nanoscale Dynamics*. (Springer Series in Solid-State sciences).
32. Chen, W., Chen, C. & Guo, L. Field-dependent low-field enhancement in effective paramagnetic moment with nanoscaled Co₃O₄. *J. Appl. Phys.* **108**, 073907 (2010).
33. Hyun, J. K., Zhang, S. X. & Lauthon, J. L. Nanowire Heterostructures. *Annu. Rev. Mater. Res.* **43**, 451–479 (2013).
34. Okamoto, S. & Millis, A. J. Electronic reconstruction at an interface between a Mott insulator and a band insulator. *Nature* **428**, 630–633 (2004).
35. Blaha, P., Schwarz, K., Madsen, G. K. H., Kvasnicka, D. & Luitz, J. WIEN2k, An augmented plane wave plus local orbitals program for calculating crystal properties. Schwarz, K. Technical University Wien, Austria (ISBN 3-9501031-1-2) (2001).
36. Schwarz, K. & Blaha, P. Solid state calculations using WIEN2k. *Comp. Matter. Sci.* **28**, 259 (2003).
37. Perdew, P., Burke, K. & Ernzerhof, M. Generalized gradient approximation made simple. *Phys. Rev. Lett.* **77**, 3865 (1996).
38. Anisimov, V. I., Solovyev, I. V., Korotin, M. A., Czyzyk, M. T. & Sawatzky, G. A. Density-functional theory and NiO photoemission spectra. *Phys. Rev. B* **48**, 16929 (1993).

Acknowledgments

We thank B. Rodriguez-Gonzalez for additional TEM measurements not shown here. R.D.B., M.F. and Z.A.L. acknowledge financial support from the European Research Council Advanced Grant “IMAGINE”. V. S. acknowledges the financial support from the Xunta de Galicia (Regional Government, Spain) project 10PXIB312260PR. R. P., D.D. and M.M. acknowledge financial support from the German Science Foundation SFB/TR80.

Author contributions

N.F.T. and S.L.V. synthesized the samples. A.K. and Z.A.L. performed the TEM analysis. Z.A.L., M.S. and M.F. conducted the magnetic measurements and analysis. M.M. and D.D. performed the DFT calculations under the guidance of R.P., R.P., V.S., R.D.B. and M.F. supervised the experiments and analyzed the data. Z.A.L., V.S., R.D.B., R.P. and M.F. wrote the manuscript. All authors contributed to the results and discussed the manuscript.

Additional information

Supplementary information accompanies this paper at <http://www.nature.com/scientificreports>

Competing financial interests: The authors declare no competing financial interests.

How to cite this article: Li, Z.-A. *et al.* Electrostatic doping as a source for robust ferromagnetism at the interface between antiferromagnetic cobalt oxides. *Sci. Rep.* **5**, 7997; DOI:10.1038/srep07997 (2015).



This work is licensed under a Creative Commons Attribution-NonCommercial-NoDerivs 4.0 International License. The images or other third party material in this article are included in the article's Creative Commons license, unless indicated otherwise in the credit line; if the material is not included under the Creative Commons license, users will need to obtain permission from the license holder in order to reproduce the material. To view a copy of this license, visit <http://creativecommons.org/licenses/by-nc-nd/4.0/>